Effect of Hydrostatic Pressure on the 3D Porosity Distribution and Mechanical Behavior of a High Pressure Die Cast Mg AZ91 Alloy

FEDERICO SKET, ANA FERNÁNDEZ, ANTOINE JÉRUSALEM,
JON M. MOLINA-ALDAREGUÍA, and MARÍA TERESA PÉREZ-PRADO

A limiting factor of high pressure die cast (HPDC) Mg alloys is the presence of porosity, which has a detrimental effect on the mechanical strength and gives rise to a large variability in the ductility. The application of hydrostatic pressure after casting is known to be beneficial to improve the mechanical response of HPDC Mg alloys. In this study, a combined experimental and simulation approach has been developed in order to investigate the influence of pressurization on the 3D porosity distribution and on the mechanical behavior of an HPDC Mg AZ91 alloy. Examination of about 10,000 pores by X-ray computed microtomography allowed determining the effect of hydrostatic pressure on the bulk porosity volume fraction, as well as the change in volume and geometry of each individual pore. The evolution of the 3D porosity distribution and mechanical behavior of a sub-volume containing 200 pores was also simulated by finite element analysis. Both experiments and simulations consistently revealed a decrease in the bulk porosity fraction and a bimodal distribution of the individual volume changes after the application of the pressure. This observation is associated with pores containing internal pressure as a result of the HPDC process. Furthermore, a decrease in the complexity factor with increasing volume change is observed experimentally and predicted by simulations. The pressure-treated samples have consistently higher plastic flow strengths.

I. INTRODUCTION

REDUCING the weight of transportation vehicles is a world trend aiming to diminish the emissions of greenhouse gases and the amount of required fuel. Magnesium (Mg) alloys are key light-weighting materials,[1–4] as their specific strength is one of the highest among all structural metals. Despite the intense research efforts devoted over the last decade to understand the physical metallurgy of Mg alloys, the design of optimized processing routes that give rise to stable microstructures with predictable mechanical properties under service conditions still requires further advances in this area.

High pressure die casting (HPDC) is the leading processing technology for Mg components in the automotive industry as it allows forming parts with complex geometries in one single operation with a limited cost. In HPDC, the molten metal is injected into the die at a high speed until the cavity is completely filled. In order to reduce the volume fraction of pores and casting defects, a pressure of approximately 40 to 50 MPa (400 to 500 bar) is subsequently applied and withdrawn only when the solidification process is complete. The heat released by the part is mostly eliminated through the casting-die interface.[5] Finally, the part is rapidly removed from the die. The most common Mg die cast alloys belong to the magnesium-aluminum series AM60 (Mg-6wt pctAl-0.5wt pctMn) and AZ91 (Mg-9wt pctAl-1wt pctZn).

Even though HPDC was invented more than a 100 years ago, relatively few studies relating the casting parameters to the resulting microstructures exist to date, e.g., References 6 through 9. This is motivated by the large cost of setting up and maintaining HPDC facilities in a research laboratory. A large number of studies have tried to relate HPDC microstructures to their mechanical behavior.[10–22] In general, it is agreed that porosity is the microstructural feature that has the most deleterious effect on the mechanical properties. In particular, the presence of pores gives rise to fracture at smaller strains than in their wrought counterparts. Furthermore, the current impossibility to reproduce three-dimensional (3D) pore distributions in different HPDC cycles leads to a large variability in the tensile ductility of different

FEDERICO SKET, is with the IMDEA Materials Institute, C/ Eric Kandel 2, 28906, Getafe, Madrid, Spain. Contact e-mail: federico.sket @imdea.org ANA FERNÁNDEZ, Postdoctoral Researcher, formerly with the Physical Metallurgy Department, IMDEA Materials Institute, is now with the Laboratory of Mechanical Metallurgy, Institute of Materials at the EPFL, Lausanne, Switzerland. ANTOINE JÉRUSALEM, Associate Professor, formerly with the IMDEA Materials Institute, is now with the Department of Engineering Science, University of Oxford, Parks Road, Oxford, OX1 3PJ, UK. JON M. MOLINA-ALDAREGUÍA, Senior Researcher, is with the Micro- and Nano-Mechanics Department, IMDEA Materials Institute. MARÍA TERESA PÉREZ-PRADO, Senior Researcher, is with the Physical Metallurgy Department, IMDEA Materials Institute.

components, thus constituting a serious limiting factor for the wide commercialization of Mg HPDC parts. Fracture has been reported to initiate at the largest microvoids[19] and at porosity segregation zones.[17] It has been proposed that tensile ductility is not related to the bulk volume fraction of pores, but to the area fraction of the pores at the fracture surface.[13–16,20,21]

Several studies have aimed at modeling the correlation between ductility and porosity.[10–12,22] Some have attempted to include 3D information of the porosity distribution into models of cast alloys.[23–25] The 3D geometry of the pores was measured using X-ray computed tomography (XCT) techniques or by serial sectioning combined with metallographic observations. In Reference 23, a significant fraction of pores is measured and the methodology to include this fraction in a finite element (FE) mesh is described. In Reference 24, a single pore is taken into account. Vanderesse *et al.*[25] utilize a relatively large microstructural volume of a cast aluminum alloy as an input for FE calculations. Further work is clearly needed in this area if realistic models of HPDC Mg alloys with good predictive capability are to be developed.

It is known that porosity and its negative effects on ductility might be reduced by applying a hydrostatic pressure.[26,27] Biner *et al.*[26] evaluated the effects of hydrostatic pressures up to 1104 MPa (11,040 bar) on the densification of iron compacts with porosity levels ranging from 0.3 to 11.1 pct. The decrease in porosity resulting from pressurization was more pronounced in samples with higher initial volume fraction of pores. The variation of the porosity level with the applied hydrostatic pressure was found to agree well with a modified Gurson's model[28,29] including internal pressure in gas pores. Uniaxial deformation under pressure has also been found to result in higher tensile ductilities due to the progressive suppression of macrovoid formation within necked regions.[27,30,31] At sufficiently high pressures, the fracture mode was observed to change into a shear-dominated mechanism.

In this work, an approach to reduce the detrimental effect of porosity in a high pressure die cast AZ91 Mg alloy by applying a hydrostatic pressure after HPDC processing is investigated. The effect of the pressure treatment on the 3D porosity distribution and on the mechanical behavior of the samples is studied using an experimental–computational methodology. The 3D distribution of pores before and after the pressure treatment is analyzed by XCT. A relatively large bulk fraction of pores reconstructed from XCT experimental measurements is used as an input for a FE model. This model is ultimately utilized to simulate and analyze the effect of pressure on the 3D pore distribution as well as on the mechanical response of the material.

II. EXPERIMENTAL DETAILS

A. *Material and Process*

An AZ91 Mg alloy was HPDC processed into a dog-bone-shaped die. The geometry and dimensions of the castings can be observed in Figure 1. Since, as it will be
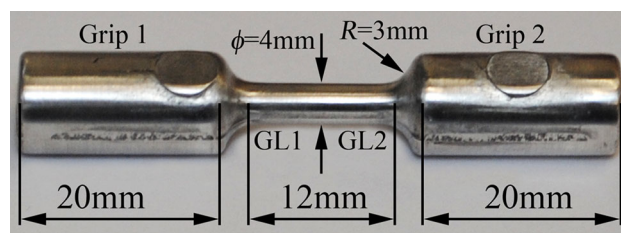

Fig. 1—Sample geometry of the Mg AZ91 dog-bone shaped casting fabricated by HPDC.

seen later, the porosity distribution is highly dependent on the location in the cast specimen, four representative regions have been identified and labeled in Figure 1 as "Grip 1", "Grip 2", "GL1" (the region of the gage length closer to Grip 1) and "GL2" (the region of the gage length closer to Grip 2). Multiple specimens were prepared using the following processing conditions. The molten material was injected at a liquid alloy temperature of 903.15 K to 943.15 K (630 °C to 670 °C) and a gate velocity of 8 to 9 m/s, using a servo-hydraulic HPDC computer-controlled machine. The injection pressure was 40 to 50 MPa (400 to 500 bar) and the mold temperature was set in the range of 463.15 K to 503.15 K (190 °C to 230 °C).

The microstructure of the as-received material was analyzed by optical microscopy in an Olympus BX51 optical microscope. The microstructure is consistent with previous observations of HPDC AZ91 castings.[32] It is formed by α-Mg "islands" (light gray) surrounded by β-phase $Mg_{17}Al_{12}$ particles (dark gray). Figure 2 includes several optical micrographs illustrating the microstructure at different magnifications. Figures 2((a) and (b)) reveal that the β-phase is homogeneously distributed throughout the microstructure. Both gas and shrinkage pores are present (selected examples are labeled in Figure 2). The former have a large size variation ranging from a few micrometers up to 200 μm in diameter. Shrinkage pores were found isolated as well as emanating from the gas pores. In Figure 2(c), some grains are visible in the vicinity of a pore. The average size of such grains is about 10 μm. It can be seen that grains are in general smaller than the dendrite width.

A pressure treatment of 600 MPa (60 bar) at room temperature [293.15 K (20 °C)] during 10 minutes was first applied to a 1.8 mm diameter and 6 mm long cylinder extracted from Grip 1, using a Hiperbaric 420 machine from Hiperbaric S.A. A disk of 1.8 mm in diameter and 820 μm in thickness corresponding to the central part of this cylinder was examined by XCT (as described in more detail in Section II–B) before and after pressurization in order to evaluate the effect of pressure on the evolution of the porosity distribution. The same pressure treatment was then applied to several HPDC dog-bone-shaped castings with the aim of investigating the effect of pressure on the mechanical behavior before and after pressurization.

B. *X-Ray Tomography Inspection*

Quantitative information of the 3D porosity distribution was obtained by means of XCT using a Nanotom

(a) Gas pore
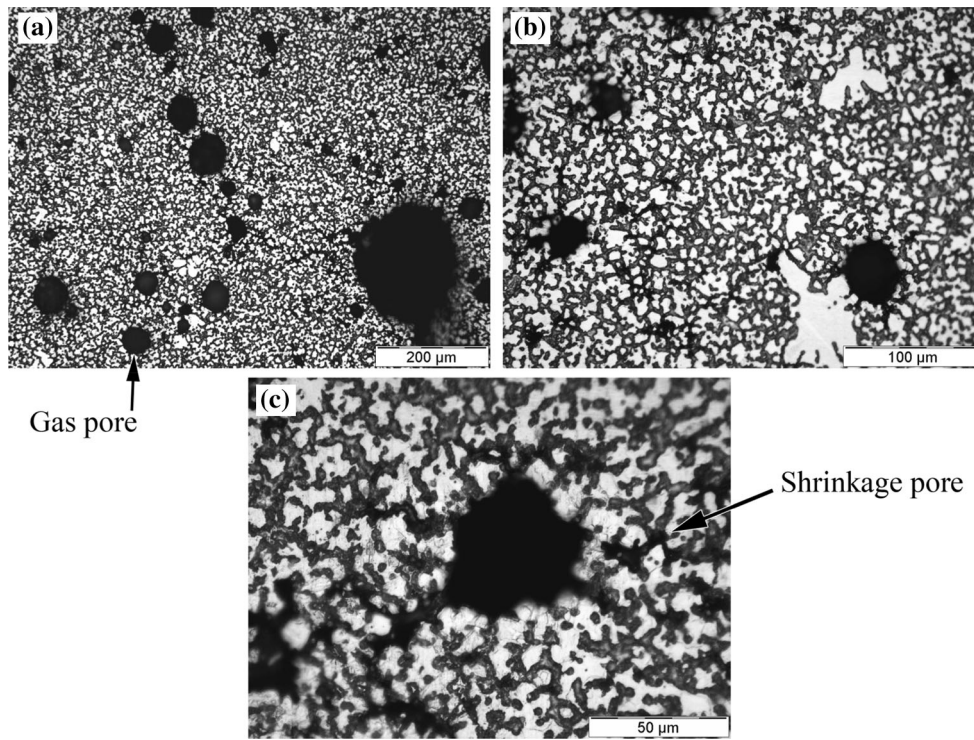
(b)

(c) Shrinkage pore

Fig. 2—Microstructure of the as-HPDC AZ91 Mg casting at different magnifications; the micrographs were taken in Grip 1.

160NF tomograph from Phoenix. All the tomographic measurements were performed utilizing a tungsten target. Five as-HPDC dog-bone-shaped specimens were first inspected at low resolution to identify qualitatively the different porosity levels throughout the samples. The conditions for the collected low resolution tomograms were 130 kV, 90 μA, 1000 projections, and 500 ms exposure time. The pixel size was set to 21.7 μm. A second measurement at a higher resolution of 4.9 μm pixel size, 90 kV, 120 μA, 2000 projections, and 500 ms exposure time was performed on different parts of the samples to better identify porosity. Finally, in order to obtain the highest possible resolution, the cylinder of 1.8 mm in diameter and 6 mm in length, described in the previous section, was machined out of the high porosity region (Grip 1) and the central part of this cylinder (a disk of 1.8 mm in diameter and 820 μm in length) was measured with a pixel size of 1 μm, 90 kV, 100 μA, 2000 projections, and 750 ms exposure time. This cylinder was then subjected to a hydrostatic pressure of 600 MPa (60 bar) at room temperature (293 K or 20 °C) during 10 minutes and the same disk was measured again under the same conditions by XCT in order to evaluate the influence of the applied pressure on each single pore. All the tomograms were reconstructed using an algorithm based on the filtered back-projection procedure for Feldkamp cone beam geometry.[33]

C. Image Processing and Void Tracking

Identification of the cavities was carried out by selection of the voxels as belonging either to a void or to the bulk matrix material based on their gray level.

Prior to the segmentation of cavities, all the slices forming the volume were equalized to have a homogeneous gray level of the matrix along the volume. The cavity segmentation procedure used was based on the local variance method from Niblack applied to each slice, adapting the threshold according to the mean and standard deviation of the peak belonging to the matrix material.[34] For the two reconstructed samples (before and after the hydrostatic pressure treatment), only cavities having a volume larger than 200 voxels (equivalent radius of ~3.6 μm) were selected after segmentation for analysis. This lower limit was chosen according to Reference 35, which showed that an ellipsoid can be well approximated by structure larger than $5 \times 5 \times 5$ (125) voxels. The complexity factor (CF) parameter[36] was used to characterize the cavity shape. The CF is related to the exclusion volume resulting from the intersection of the real cavity with its equivalent ellipsoid (same volume and moment of inertia). The CF can be calculated as:

$$CF = \frac{V_1 + V_3}{V_C}, \qquad [1]$$

where $V_C = V_1 + V_2$ is the volume of the cavity, composed of the volume of the cavity outside the equivalent ellipsoid (V_1) and the volume of the cavity inside the ellipsoid (V_2), and V_3 is the volume of the ellipsoid which is not occupied by the cavity.

The effect of pressure on the volume and shape of the pores was analyzed by tracking each individual pore in the disk before and after pressurization. Prior to void tracking, the two volumes of the disk, measured with the highest resolution, were translated and rotated using the

Image Fusion module of MedINRIA for image registration.[37] The registration was performed using manual landmarks and rigid body options to perform translation and rotation, but not scaling. The cavities found in the initial volume were tracked in the pressure-treated volume using an in-house image registration algorithm developed in Matlab and based on the phase-correlation method centered on each cavity.[38,39] For that purpose, an area of interest (AOI) centered on the maximum area of the selected cavity was chosen. The AOI size was sufficiently large to contain a few extra features (neighbor cavities or highly absorbing particles) to improve the correlation coefficient in the local area. By fulfilling a proximity criterion, based on a minimum distance from the center of gravity of the initial cavity to any pixel of the pressure-treated cavity, the cavities were considered as found or lost.

After the pressure treatment, gas pores linked by a crack or a shrinkage pore may in some cases lose such link as a result of closure of the linking crack or shrinkage pore. In this case, a single cavity in the initial state splits into two or more cavities in the final state. This effect was considered by detecting the number of such final state cavities, called "predecessor" cavities,[38] and was taken into account in the evaluation of cavity evolution by removing them from the analysis.

D. Mechanical Testing

In order to study the effect of the applied pressure on the mechanical behavior of the HPDC AZ91 alloy, 12 cylindrical specimens of about 3 mm in diameter by 4.5 mm in length were extracted from a high porosity region (Grip 1) of the HPDC dog-bone specimens (six from non-treated samples and six from pressurized specimens) and were tested under uniaxial compression at room temperature in an electromechanical universal testing machine (Instron 3384) at constant strain rate of 10^{-4} s^{-1}. The load was monitored with a 10 kN cell.

E. Finite Element Analysis

The influence of the applied pressure on the 3D porosity distribution and on the mechanical behavior of the HPDC AZ91 alloy was analyzed by FE. The FE model was built from a $300 \times 300 \times 300$ μm^3 (1 pixel = 1 μm^2) tomographic sub-volume extracted from the high resolution XCT measurement of the 1.8 mm diameter and 820 μm-thick disk (Figure 3). This sub-volume contained ~200 complete pores (i.e., not in contact with the sub-volume faces).

The FE model was built as follows. A surface mesh was created in StereoLithography (STL) format from the tomographic binarized data using VGStudio Max software.[40] A similar methodology was used in Reference 41 for cellular materials. The number of surface elements was set to achieve an optimal resolution in order to capture the shape of the pores as accurately as possible. The STL surface-meshed volume was then imported into Hypermesh[42] and meshed with 792,681 quadratic tetrahedral elements (1,129,194 nodes). In order to reduce the number of elements the finest mesh
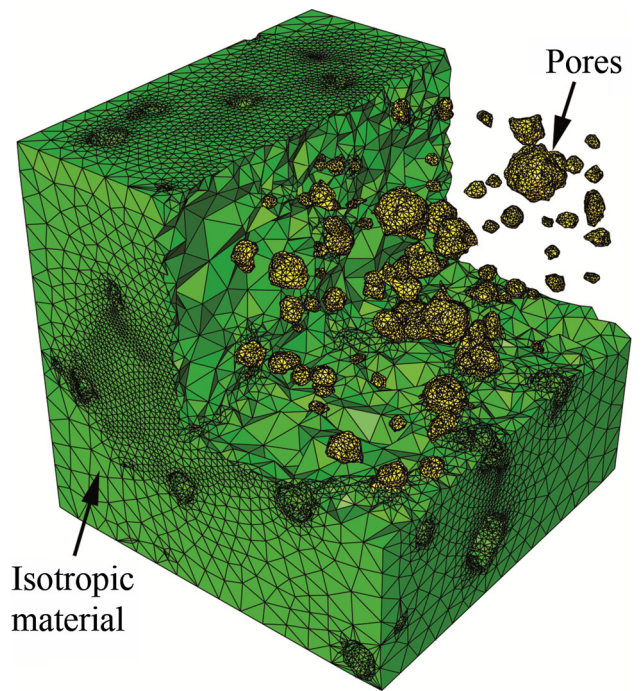

Fig. 3—FE mesh of the selected tomographic sub-volume geometry. A sector of the pore-free mesh was removed for visualization purposes (Color figure online).

in the neighborhood of the pores was gradually coarsened toward pore-free regions. The meshed volume was finally exported to the FE program Abaqus 6.11/Standard[43] in order to carry out the simulations.

The behavior of the bulk material was described using standard J_2 plasticity with linear isotropic hardening. Note that this implies that the crystallographic microstructure (grain size, texture, etc.) is not accounted for (see discussion in Section IV). Accordingly, the yield stress σ_y is defined as:

$$\sigma_y\left(\bar{\varepsilon}^{pl}\right) = \sigma_0 + H\bar{\varepsilon}^{pl}, \qquad [2]$$

where σ_0 is the initial yield strength, $\bar{\varepsilon}^{pl}$ is the equivalent plastic strain and H is hardening modulus.

A Young's modulus of 44.8 GPa and a Poisson's ratio of 0.35 were used as the elastic properties of the AZ91 Mg alloy.[44] The initial yield stress σ_0 and the hardening parameter H were obtained from uniaxial compression tests of cylinders of 4 mm in diameter and 6 mm in length machined out from a very low porosity region (GL2). The average porosity in GL2 was smaller than 1 pct. Previous studies, e.g., Reference 45, have shown that these parameters are insensitive to porosity below such levels, thus suggesting that the proposed approximation is reasonable. The tests were done with an electromechanical universal testing machine (Instron 3384) at constant strain rate of 10^{-4} s^{-1} and the load was monitored with a 10 kN load cell. Figure 4 shows the experimental and simulation results for $\sigma_0 = 160$ MPa and $H = 2200$ MPa.

The final model using the mesh shown in Figure 3 and the constitutive model calibrated in Figure 4 was subjected statically to a hydrostatic pressure of 600 MPa
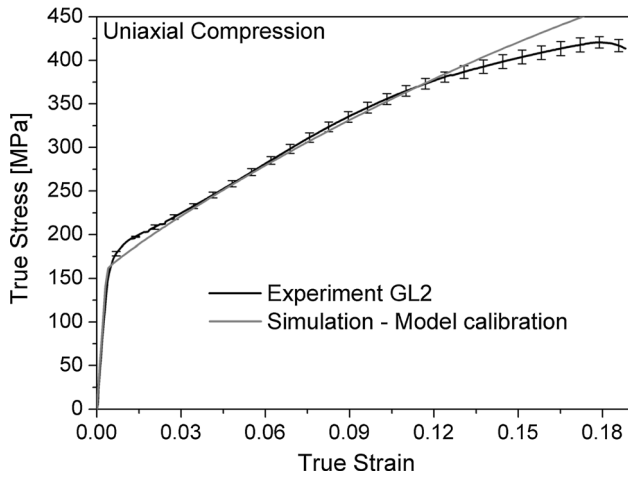
Fig. 4—Uniaxial compression true stress–true strain curves. Experimental data and model calibration.

(60 bar) followed by relaxation. The effect of pressure on the 200 complete pores was tracked. The mechanical response of the sub-volume before and after the simulated pressure treatment was ultimately analyzed by simulating a uniaxial compression test. In both cases, the two compressed faces were laterally constrained.

III. RESULTS

A. Experimental Results

1. Qualitative analysis

Figure 5 illustrates the low resolution tomographic reconstruction of the complete dog-bone initial sample, the high resolution reconstruction of the disk from the cylinder subjected to the high pressure treatment (extracted from Grip 1) before the application of the pressure, and the sub-volume of $300 \times 300 \times 300 \ \mu m^3$ used in the FE model. The low resolution reconstruction exhibits different void sizes and concentrations along the sample axis. In particular, larger voids and a higher void density can be found in the grips. Grip 2 contains mostly globular pores while in Grip 1 a large concentration of cracks and shrinkage pores can additionally be observed. The gage length also presents a heterogeneous spatial distribution of pores. In particular, the pore density is higher in the region close to Grip 1 (see Figure 5). The void volume fraction varies in different regions of the sample from an average value of about 9 pct (range 5 to 15 pct) in the grips to 0.7 pct (range 0.5 to 1.0 pct) in the gage length. Even in the smallest disk volume measured by high resolution tomography the void volume fraction varies in the untreated specimen from 5 to 13.4 pct.

Preliminary two-dimensional inspection of the reconstructed tomographic slices before and after the application of the pressure exhibits a reduction in the number of pores, in the pore size, as well as in the occurrence of changes in the pore geometries. As an example, Figures 6((a) and (b)) show two reconstructed slices, before and after the pressure treatment, respectively, of the same cross section of the HPDC specimen after a correlation procedure. Two areas within these cross sections have been enlarged and are shown in Figures 6((c) and (d)). Most of the pores shown in Figure 6(d) are smaller than their counterparts prior to treatment in Figure 6(c) and their shapes have also been altered. Finally, it can be noted that the thin wall separating the central large pore from its neighbor (indicated by the arrows) undergoes significant plastic strain and is wider after the pressure treatment. This effect was frequently observed in the inspected volume.

The 3D effect of the pressure treatment on the pores can be better appreciated in Figures 7((a) through (c)). The sub-volume extracted for the FE model was selected as a representative volume element (RVE) of the overall disk. The size of this RVE was chosen as a balance between representativeness and visualization, since the large amount of pores contained in the disk would hinder the 3D visualization. The porosity distribution before and after pressure treatment can be seen in Figures 7((a) and (b)), respectively. The reduction in pore volume is visually noticeable in the majority of the pores by superposition of both volumes in Figure 7(c). A closer inspection of Figures 6 and 7 shows that the hydrostatic pressure affects more strongly the cracks or shrinkage pores arising from the surface of the globular gas pores, by closing them completely, within the limits of the resolution used in the XCT studies (some are indicated by arrows in Figure 7). This is expected as high stresses normally concentrate at the acute angles formed by the cracks around the pores, causing a larger volume reduction and shape alteration.

2. Quantitative analysis of pore volume and shape change

The combination of XCT with powerful image analysis techniques allows for a statistical evaluation of the evolution of a large number of cavities subjected to the pressure treatment, using the procedure explained in Section II–C. Only cavities composed of more than 200 voxels were considered in the analysis. A total of 17,649 cavities larger than 8 voxels were found in the initial volume, while 13,549 cavities remained after the treatment. From the latter set, it was possible to track 9689 cavities larger than 200 voxels which fulfilled the proximity criterion and only had one predecessor. The volume change of the initial cavities which split in more than one predecessor cavity can be obtained by comparing the sum of volumes of the predecessor's cavities to the initial one. However, they were not considered in this analysis for simplicity. Only 2164 cavities had split in more than one predecessor cavity.

Figure 8(a) shows the histogram of the relative volume change ($\Delta V/V_0$) for the 9689 tracked pores. The distribution is bimodal showing a first peak at around 6 pct, and a second one at 37 pct, the latter being fairly symmetric and relatively wide. The first peak is composed of 1742 cavities, while 7947 cavities belong to the second one, *i.e.*, 78 pct of the cavities have experienced an average volume change of 37 pct. This arguably counterintuitive bimodal distribution is thought to be a reasonable indication that some pores (belonging to the first peak) contain pressurized gas
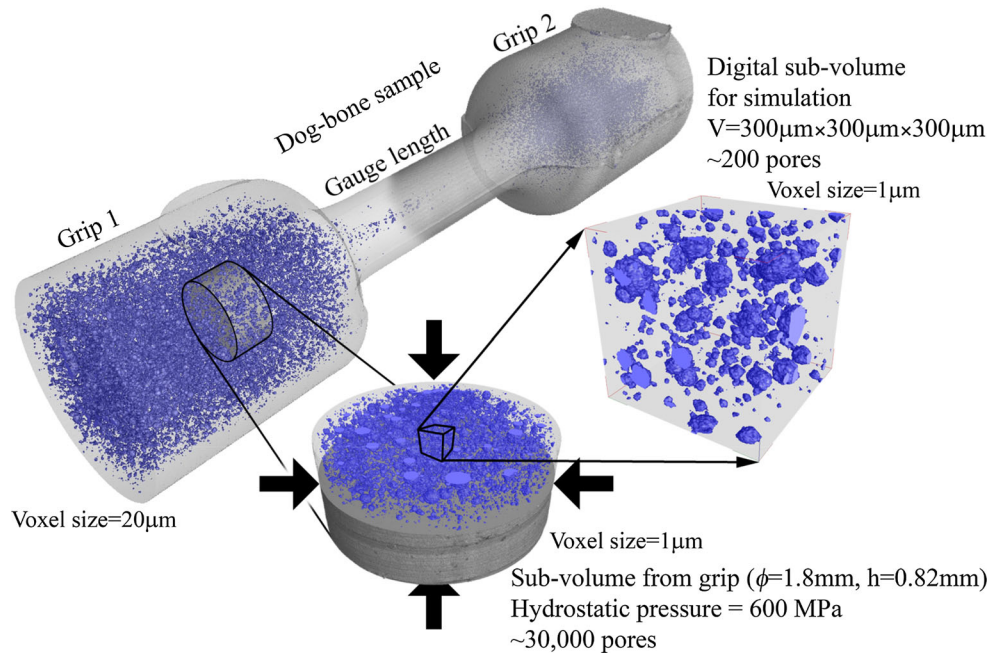
Fig. 5—Low resolution tomographic reconstruction of the complete dog-bone casting, high resolution reconstruction (initial state) of the cylindrical volume subjected to the pressure treatment and of the sub-volume of $300 \times 300 \times 300~\mu m^3$ used in the FE model (Color figure online).
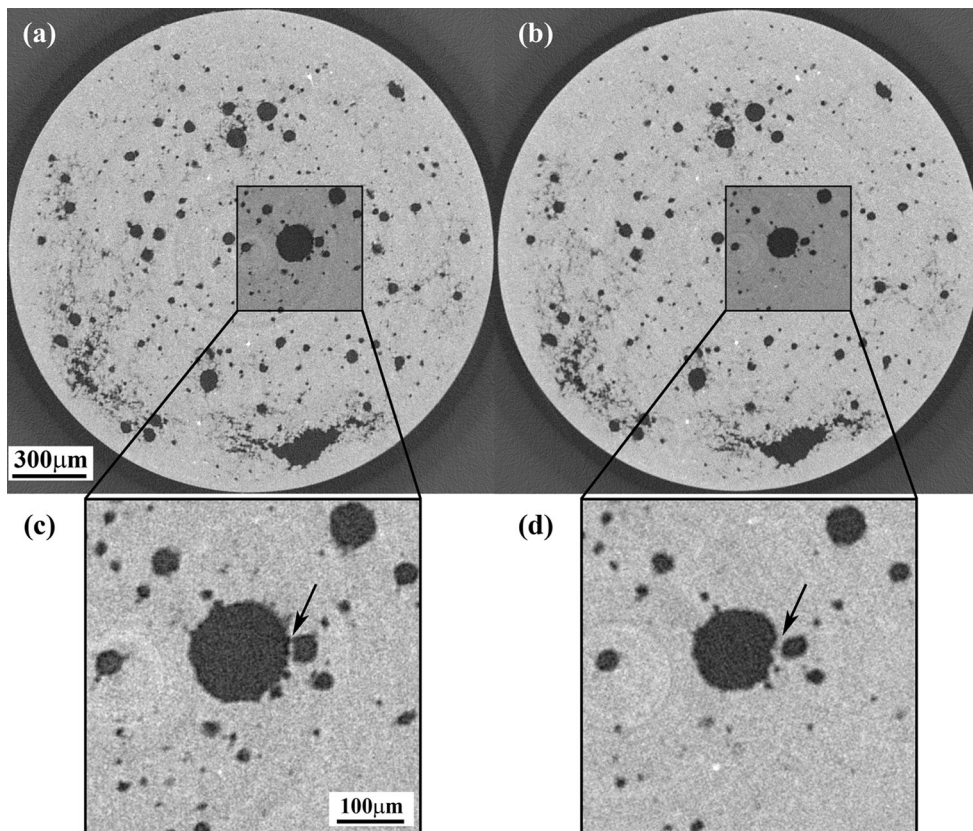

Fig. 6—Reconstructed cross-sectional views of the same slice: (*a*) before and (*b*) after the pressure treatment. Magnified region at the largest area of the central pore: (*c*) before and (*d*) after the pressure treatment.
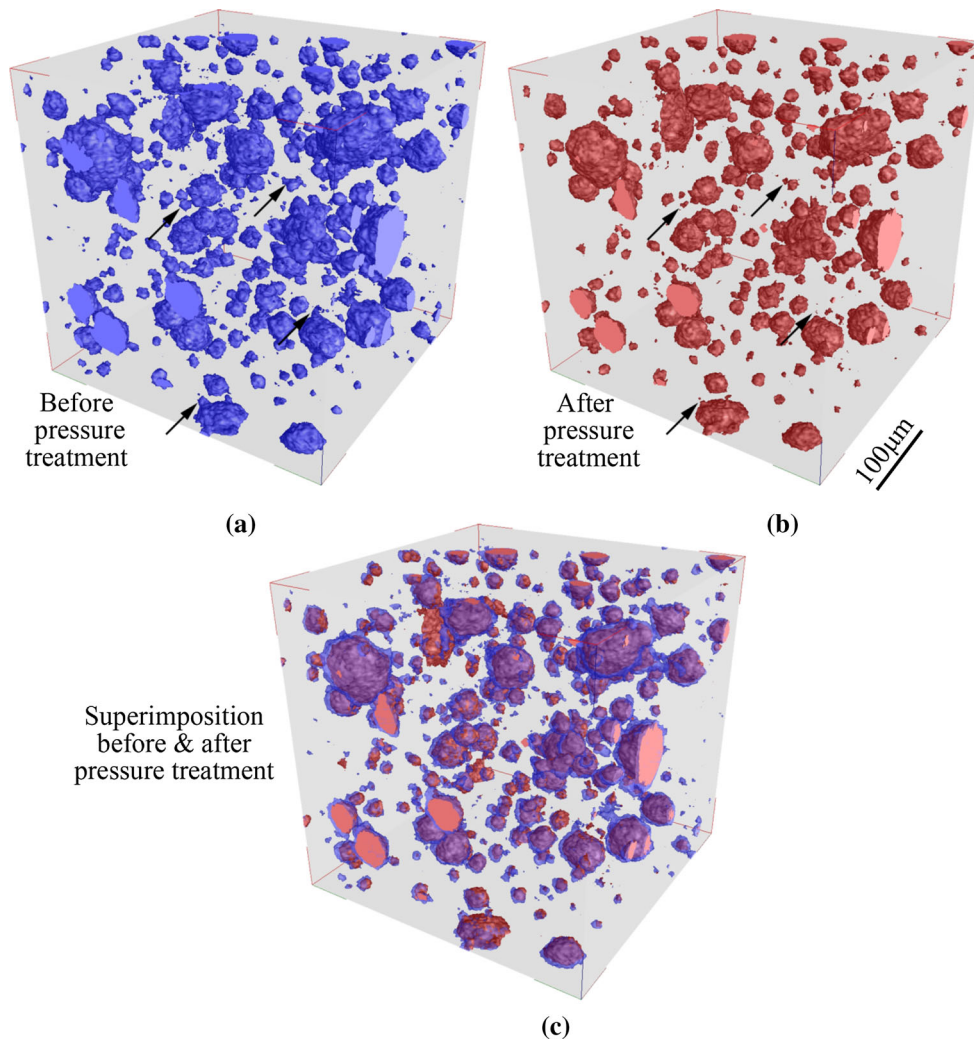
Fig. 7—3D reconstruction of the sub-volume extracted for simulation purposes: (*a*) before and (*b*) after the pressure treatment. (*c*) Superposition of volumes from (a) and (b) with initial pores (before treatment) set to semitransparent (Color figure online).
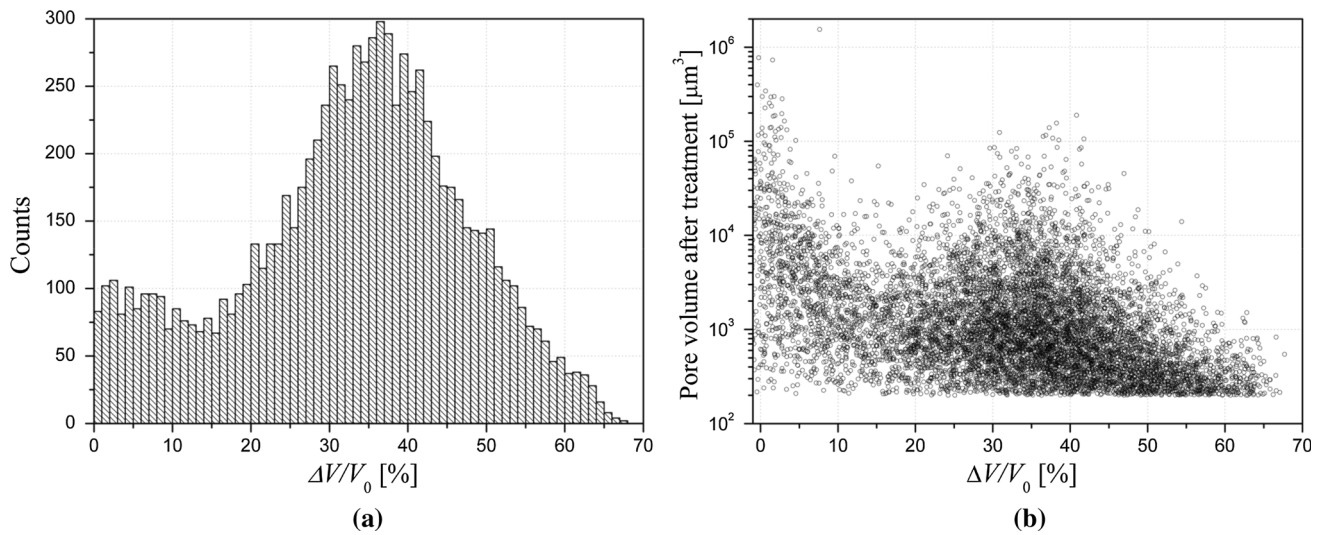

Fig. 8—(*a*) Histogram of the relative volume change ($\Delta V/V_0$) of the 9689 tracked cavities. (*b*) Pore volume after pressure treatment *vs* relative volume change.

arising from the high pressure die casting process, thus preventing them from further shrinking. The average volume change of the whole cavity population is 33 pct. In an attempt to better understand the effect of pressure on the pore volume change, the pore volume after the pressure treatment *vs* the relative volume change is plotted in Figure 8(b). It can be seen that volume changes below 15 pct are associated to a wide range of pore sizes, suggesting that pores with internal pressure have a large variety of sizes. Volume changes larger than 45 pct correspond mainly to pores whose volume is less than $\sim$3500 μm^3. Additionally, the pores with volumes larger than 5000 μm^3 (belonging to the second peak) undergo an average change of 33 pct, see Figure 8(b), while smaller pores undergo changes within the whole range.

The ellipsoid fitting procedure for pores allows for the evaluation of pore shape. In this study, we have focused our attention on the complexity factor parameter, CF, described above.[36] Figure 9(a) is a histogram of the relative CF change ($\Delta CF/CF_0$), where ΔCF is the difference between the initial and the final CF. The maximum of the relative CF change is centered at $\sim$0 pct but the $\Delta CF/CF_0$ distribution is slightly asymmetric toward negative values. A negative change in $\Delta CF/CF_0$ indicates that the pores become more irregular after the pressure treatment. The variation of $\Delta CF/CF_0$ with $\Delta V/V_0$ is shown in Figure 9(b). It can be observed that the pores that belong to the first peak of relative volume change ($\Delta V/V_0\sim$6 pct) tend to have positive values of $\Delta CF/CF_0$, *i.e.*, they tend to become more regular after pressurization. The internal pressure of these pores seems to influence their plastic deformation during pressurization, making them more regular. $\Delta CF/CF_0$ tends to subsequently decrease from positive values to negative ones (more irregular pores after the pressure treatment) as $\Delta V/V_0$ increases. For pores for which $\Delta V/V_0$ is close to 27 pct, the average $\Delta CF/CF_0$ is close to 0 pct. As $\Delta V/V_0$ becomes larger than 40 pct (corre-

sponding mainly to pores whose volume is less than $\sim$3500 μm^3, cf. Figure 8(b)), the average $\Delta CF/CF_0$ adopts increasingly more negative values.

B. *Simulation Results*

FE simulations were performed on the numerically extracted sub-volume from Grip 1 (Figures 3 and 5) following the procedure explained in Section II–E. The experimental results show a bimodal distribution of the volume change consistent with internal pressure on some of the pores formed during casting process. The pores with a volume change smaller than 15 pct were assumed to have internal pressure and 7 pores fulfilling this condition (out of $\sim$200) were identified in the simulation sub-volume counterpart. Two simulations were then carried out, with and without internal pressure in the 7 selected pores. The internal pressure in the pores was mimicked by defining a quasi-incompressible behavior of the pores (but with a negligible shear modulus), calibrated so as to capture the first peak of the relative volume change distribution at $\sim$6 pct.

Figure 10 compares the experimental relative volume change data corresponding to the pores included in the sub-volume used for simulations with the predictions of the model with and without internal pressure in the selected pores. The average experimental relative volume change is $\sim$37 pct which is consistent with the average relative volume change experienced by the larger disk-shaped sub-volume that was previously analyzed (Figure 8). The peak observed at small $\Delta V/V_0$ ($\Delta V/V_0 <$ 15 pct) in Figure 8 is also apparent in Figure 10, albeit with a significantly smaller height, since it only includes 7 pores and is lacking statistical significance. Indeed, this is equivalent to $\sim$3.5 pct of the total number of pores in the simulation sub-volume while up to 22 pct of the pores belong to this group in the larger experimentally analyzed volume. The distribution of the simulated $\Delta V/V_0$ without considering the
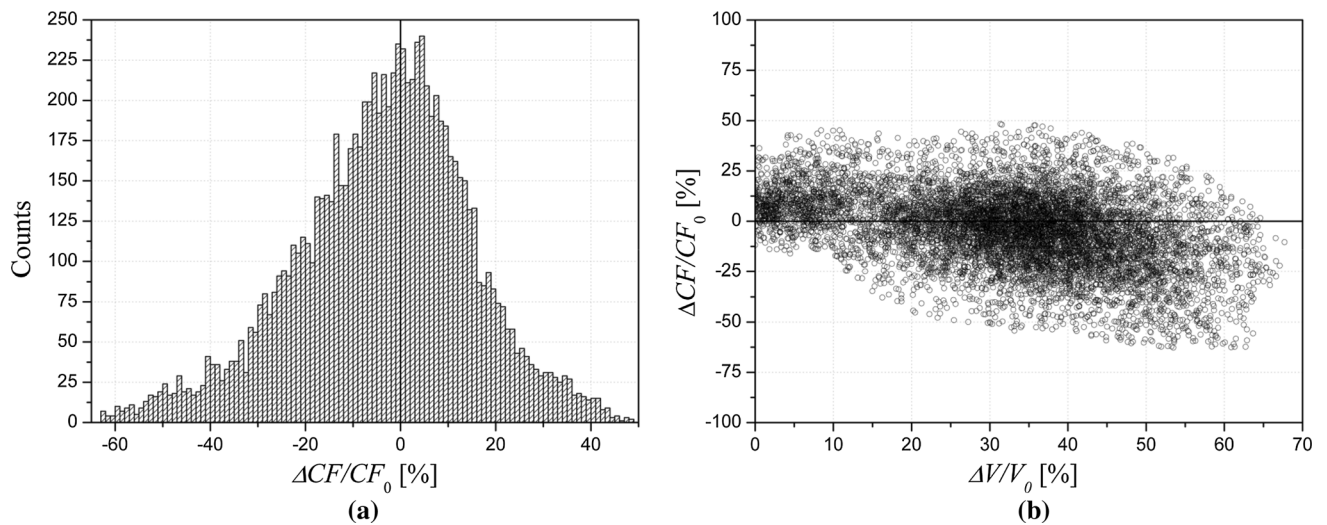

Fig. 9—(*a*) Histogram of the relative CF change ($\Delta CF/CF_0$) of the 9689 tracked cavities. (*b*) Relative CF change ($\Delta CF/CF_0$) *vs* relative volume change ($\Delta V/V_0$). Positive values of $\Delta CF/CF_0$ indicate transition to more regular pores, while negative values indicate transition to more irregular pores.

internal pore pressure consists of a single peak and the average $\Delta V/V_0$ is ~23 pct. Taking into account, the pores with internal pressure gives rise to a bimodal distribution in which the peak at low $\Delta V/V_0$ includes the same 7 pores mentioned earlier (Figure 10). The average $\Delta V/V_0$ is 23.5 pct for the simulation with internal pore pressure which is still below the 37 pct measured experimentally in the same sub-volume. Comparison between the pore volume after pressure treatment vs the relative volume change in Figure 10(b) confirms that the simulations succeed in better capturing the behavior of pores larger than 5000 μm^3, undergoing a volume change of around 33 pct, while failing at capturing the tail of pores that undergo larger volume changes, corresponding to pores whose volume is less than

~3500 μm^3. The possible reasons for this discrepancy will be discussed below.

Figure 11 compares the distributions of the relative change in the complexity factor, $\Delta CF/CF_0$, corresponding to the pores included in the simulated sub-volume, for the experiment and the simulation with and without internal pressure. The average value of $\Delta CF/CF_0$ obtained experimentally is −8 pct, while both simulations render a value of about −13 pct (Figure 11(a)). Unlike the study of $\Delta V/V_0$, simulations capture adequately the average value of CF. Both experiments and simulations show that the $\Delta CF/CF_0$ decreases as $\Delta V/V_0$ increases (Figure 11(b)), in agreement with the trend illustrated in Figure 9(b). The pores for which $\Delta V/V_0 < 15$ pct become slightly more regular after
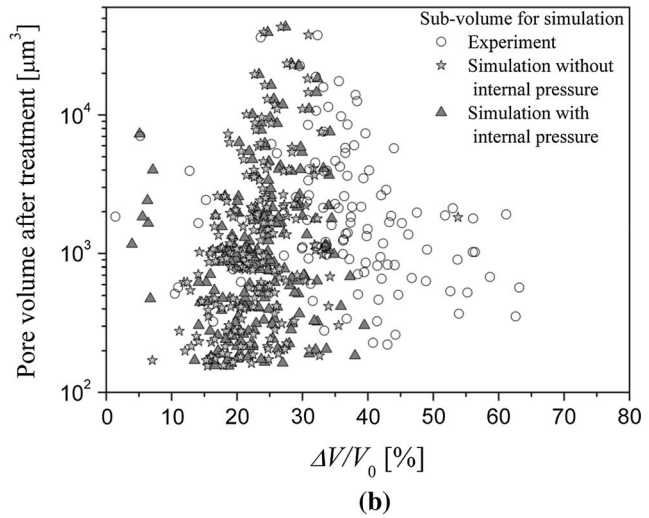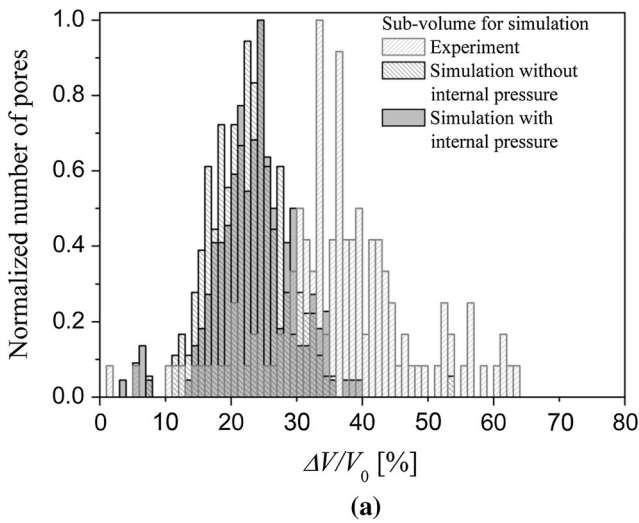

Fig. 10—Comparison between experimental and simulations results with and without internal pressure for the same sub-volume. (a) Normalized number of pores vs the relative volume change ($\Delta V/V_0$). (b) Pore volume after pressure treatment vs relative volume change ($\Delta V/V_0$).
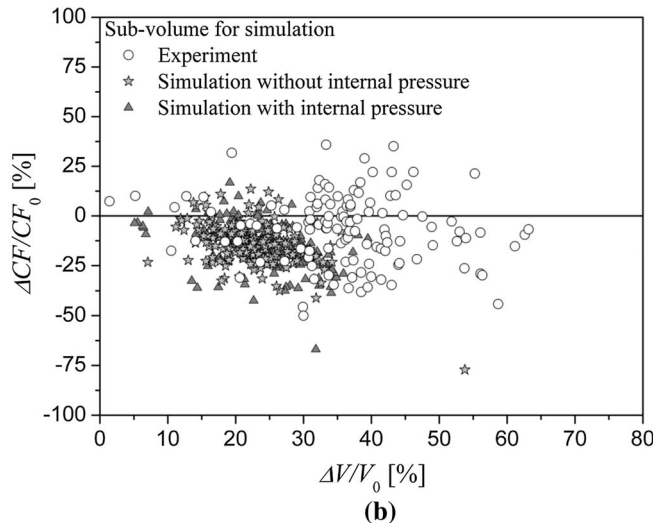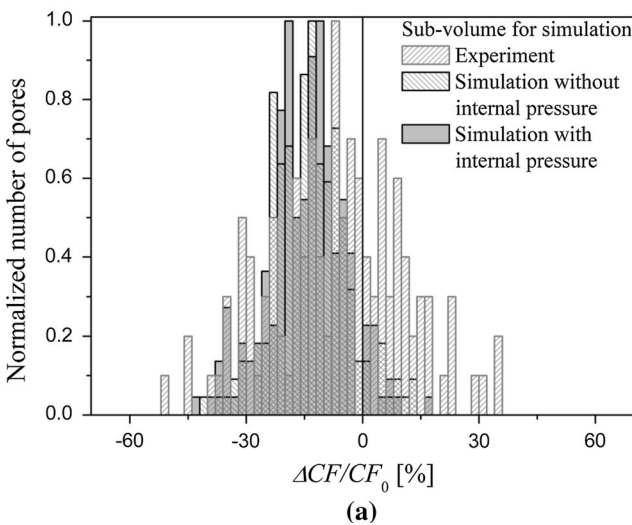

Fig. 11—Comparison of experimental results and simulations with and without internal pressure for the same sub-volume. (a) Normalized number of pores vs the relative complexity factor change ($\Delta CF/CF_0$). (b) Relative complexity factor change ($\Delta CF/CF_0$) vs relative volume change ($\Delta V/V_0$).

pressurization. This effect is also captured by the simulations performed with internal pressure in the selected pores yielding a value close to zero. The pores undergoing a larger volume change tend to adopt a more irregular geometry after the pressure treatment. Again and as it will be discussed later, the tail of the $\Delta CF/CF_0$ *vs* $\Delta V/V_0$ distribution (Figure 10(b)), formed by the pores which undergo a relative volume change larger than 40 pct, *i.e.*, those for which $\Delta CF/CF_0$ decreases more, is not captured by the model.

C. Mechanical Tests

Uniaxial compression tests were performed on both the as-received material and the pressure-treated material. The corresponding true stress-true strain curves are shown in Figure 12(a). The pressure treatment results in an increase of the stress over the whole plastic region, with an increment of 31.5 MPa. Similar strain hardening behaviors are observed before and after pressurization.

The influence of the pressure treatment on the mechanical behavior was also investigated with the FE model. The results of the simulation, shown in Figure 12(b), also reveal that the pressure treatment induces an improvement of 26.4 MPa of the flow stress over the plastic region, in close agreement with the experimental results. However, the simulations predict higher absolute flow stress values than the experimental measurements. This is undoubtedly a result of the particular pore volume fraction contained in the simulated sub-volume (Figure 5). While in the simulated sub-volume the volume fraction of pores was about 5 pct, the real pore volume fraction reached local values of up to 13.4 pct in the experimentally compressed cylinders. This naturally leads to higher simulated flow stresses but, despite these differences, the model was able to capture the beneficial effect of the pressure treatment quantitatively.

IV. DISCUSSION

The evolution of the porosity distribution of an HPDC AZ91 casting upon pressurization has been analyzed by XCT and simulated in a sub-volume of the material by FE, using the experimentally determined distribution of pores in this particular sub-volume and J_2 plasticity with linear isotropic hardening for the pore-free matrix. In general, a good agreement is found between experiments and simulations regarding the change in volume and in geometry of a large number of individual pores. The study reveals that a large fraction of pores (around 22 pct) is relatively insensitive to the pressurization treatment, presumably due the presence of internal pressure as a result of the HDPC process. The study also reveals a good agreement between experiments and simulations for pores larger than 5000 μm^3 that undergo a relative volume reduction of ~33 pct. However, XCT reveals that a significant number of pores with volumes after pressurization smaller than 3500 μm^3 undergo relative volume changes between 45 and 65 pct and these are not captured by the simulations. These same pores experience large reductions in their relative complexity factors (see Figure 11(b)), *i.e.*, they adopt more irregular shapes after the pressure treatment. An aspect that might play an important role in this discrepancy is the plastic anisotropy inherent to the hcp Mg lattice,[46] not taken into account in the model. Pores with final volumes between 200 and 3500 μm^3 undergoing relative volume changes between 45 and 65 pct have initial volumes comprised between approximately 350 and 6400 μm^3, *i.e.*, with equivalent radii between 4.4 and 11.4 μm. A close inspection of Figure 2(c) reveals that the grain size ranges from approximately 5 to 10 μm. Thus, the size of the pores that show the discrepancy is of the same order of magnitude as the grain size and are, therefore, surrounded by a limited number of grains, not exceeding about 10. These grains, depending on their
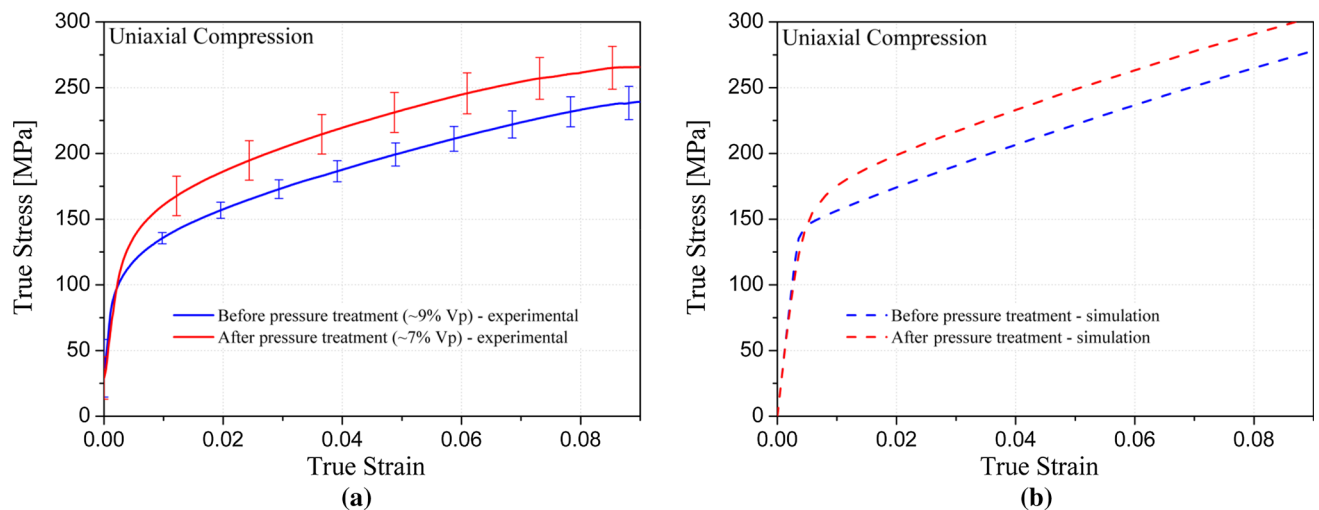

Fig. 12—Uniaxial compression response of (*a*) cylinders extracted from Grip 1 before and after the pressure treatment as measured experimentally and (*b*) the simulated sub-volume.

orientation, will undergo different amounts of plastic strain due to the inherent anisotropy of plastic deformation and the high local shear stresses build up around the pores. This can lead to larger pore volume reductions and to the more irregular pore geometries for pores with sizes in the range of the grain size. This effect is expected to be strong in Mg alloys because the critical resolved shear stresses of the different slip and twin systems in Mg alloys at room temperature might span up to 2 orders of magnitude.[47]

This study also brings the opportunity to analyze the effect of neighboring pores on the evolution of the porosity during the pressure treatment. Figure 13 shows the equivalent plastic strain field in four different cross sections of the simulated sub-volume after the hydrostatic pressure was released. As expected, the material at the pore surfaces undergoes large plastic strains and, interestingly, the strain fields of neighboring pores interact with each other, provided they are close enough. Figure 13 also reveals that the extent of the plastic strain field around a given pore increases with its size. According to the literature on void growth under hydrostatic stresses,[48] pore interactions are no longer negligible when the surface to surface distance is equivalent to the pore diameter, which is consistent with our simulations. Moreover, the experimental evidence presented in Figures 6((c) and (d)) reveals that, in the vicinity of large pores, significant plastic strain occurs in the thin

ligaments that separate these pores from their neighbors, suggesting that pores that have large neighboring pores undergo larger pore size alteration under pressure.

In order to test whether these experimental observations have any statistical significance, the extensive pore population studied here, with pore sizes ranging from 200 to 3,000,000 μm^3, was analyzed using an approach based on nearest neighbor distance. In order to account for the size of the neighboring pore, the ligament ratio, $Rw = w/(w + r_{NN})$, was computed for each pore, where w is the surface to surface (ligament) distance and r_{NN} is the radius of the corresponding neighboring pore. This parameter varies between 0 for a very small wall distance or a very large neighbor pore and 1 for a large ligament distance or a very small pore. The smaller this parameter is for a given pore, the higher the effect the neighboring pores should have on its size reduction. For instance, a small neighboring pore with a very short ligament distance is expected to affect the pore less than a large neighboring pore whose ligament distance is slightly larger, and this is reflected in a lower value of the Rw for the latter pore configuration. Only the first six neighbor pores with the minimum Rw were considered, assuming that they have a high probability of being first order nearest neighbors and that they are spatially homogenously distributed. Figure 14 shows the result of plotting $\Delta V/V_0$ as a function of Rw. The different curves correspond to different initial volume classes (ranges of
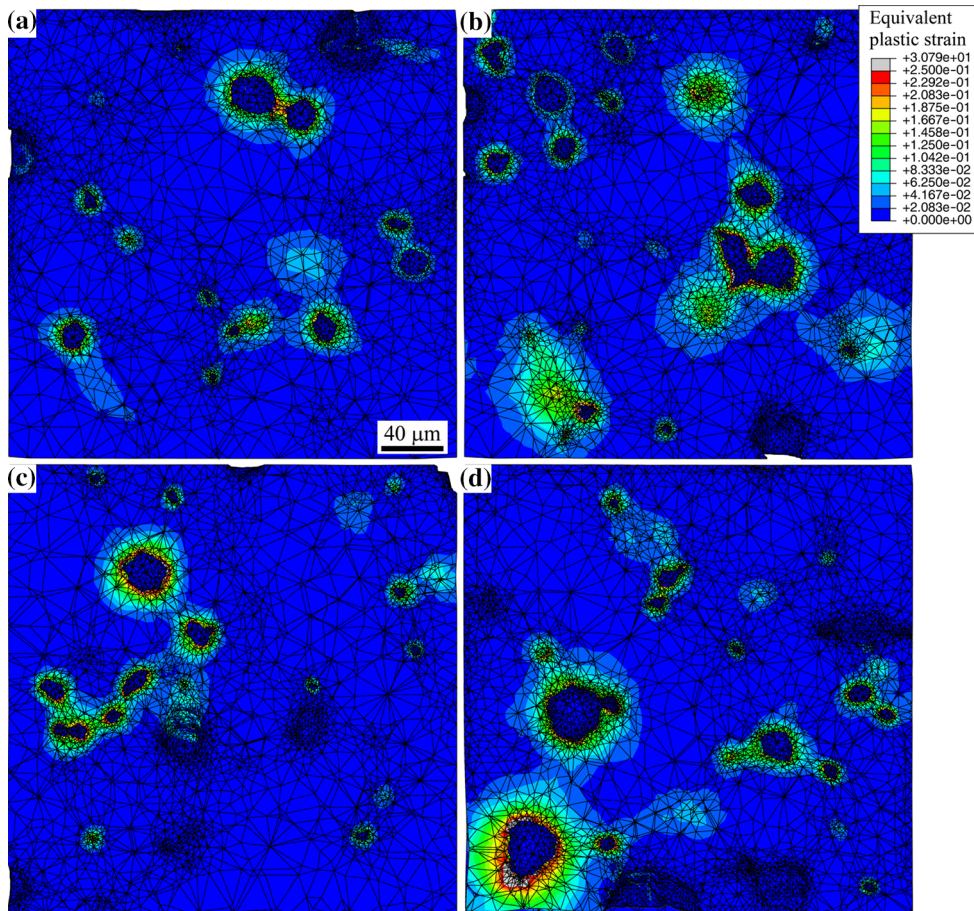

Fig. 13—Examples of the equivalent plastic strain field located around the pores after releasing the hydrostatic pressure (Color figure online).
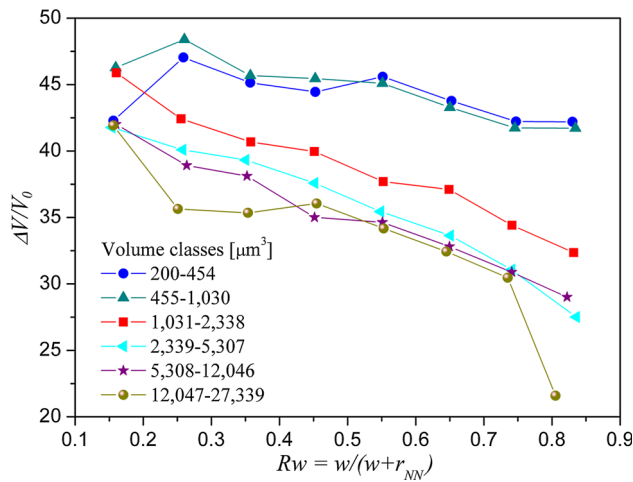
Fig. 14—Relative volume pore change ($\Delta V/V_0$) *vs* $Rw = w/(w + r_{NN})$ for several initial pore volume classes (Color figure online).

pore volumes in logarithmic scale). For values of the Rw between 0.1 and 0.25 (*i.e.*, when neighboring pores are large compared with the ligament width) all the volume classes experience a large pore size reduction $\Delta V/V_0$ of about 44 pct, indicating a strong interaction between the strain field of the pore under analysis with the ones of its neighbors. For values of the Rw higher than 0.25, *i.e.*, as the ligament width increases with respect to the size of the neighboring pore, two different trends are observed as a function of initial pore size. For pores with volumes larger than 1030 μm^3, the pore size reduction $\Delta V/V_0$ decreases as Rw increases, pointing to a smaller effect of neighboring pores. For pores with volumes up to 1030 μm^3, the pore size reduction, $\Delta V/V_0$, remains high and decreases with Rw only slightly. This is consistent with the fact that these pores correspond to pores with sizes in the range of the grain size, and therefore the local microstructure has an important effect on the pore size reduction of these small pores. As such, for Rw values of about 0.8 the $\Delta V/V_0$ of small pores reaches values close to 2 times the $\Delta V/V_0$ for large pores, in agreement with Figure 8(b).

As a consequence, this analysis reveals that the presence of neighboring pores influences significantly the pore size reduction upon pressurization. The results are in agreement with FE analysis performed by Tvergaard[49] on the interaction of pores of different sizes under high stress triaxialities, showing that smaller voids grow more rapidly than larger voids if the void volume fraction is sufficiently high (above around 0.5 pct). It is interesting to mention that the method presented in this work could also be used to study experimentally the effect of different void volume fractions on the relative volume change of voids of various sizes, especially below a radius of 3 μm, provided that a higher spatial resolution is achieved, *e.g.*, by synchrotron XCT. It has been recently stated that strain gradients could affect the rate of growth of voids with radii smaller than the characteristic length of the material[50] due to nonlocal plasticity effects. Approximate values of characteristic lengths have been sug-

gested to be in the range of 0.25 to 1 μm,[50,51] and therefore void growth should be noticeably slowed down for void radii of 2 μm and smaller. The smallest void volume considered in this study (~200 μm^3) corresponds to a radius of 3.6 μm which is still above the value where nonlocal plasticity effects are expected to occur. This is also consistent with the fact that the majority of the pores with $\Delta V/V_0 < 15$ pct (Figure 8(b)) have volumes well above 200 μm^3, thus confirming that only internal gas pressure can explain their small $\Delta V/V_0$.

V. CONCLUSIONS

This study constitutes a complex experimental-modeling approach aimed at investigating the evolution of the porosity distribution and the mechanical behavior of an HPDC AZ91 Mg alloy subjected to a hydrostatic pressure treatment. A total of 9689 pores were tracked before and after pressurization by image analysis based on XCT measurements. Conjointly, a sub-volume of the material containing 200 cavities was simulated by FE analysis, using the experimentally determined distribution of pores and an isotropic hardening for the pore-free matrix. The main conclusions drawn from this investigation are listed below.

1. Pressurization results in a decrease of the volume of the pores. The distribution of the relative volume change ($\Delta V/V_0$) is bimodal and exhibits a first peak at small values of approximately 6 pct, attributed to pores with an internal pressure arising from gas trapped during processing, and a second one at 37 pct. $\Delta V/V_0$ values as high as 65 pct (for pores after treatment with a volume of 200 μm^3) are observed to take place in the pores with the smallest initial volumes considered (571 μm^3).
2. The application of pressure also influences the pore geometry. Pores that belong to the first peak of relative volume change ($\Delta V/V_0$~6 pct) tend to have positive values of $\Delta CF/CF_0$, *i.e.*, they tend to become more regular after pressurization. $\Delta CF/CF_0$ tends to subsequently decrease from positive values to negative ones (more irregular pores after the pressure treatment) as $\Delta V/V_0$ increases. For pores for which $\Delta V/V_0$ is close to 27 pct the average $\Delta CF/CF_0$ is close to 0 pct. As $\Delta V/V_0$ becomes larger than 40 pct the average $\Delta CF/CF_0$ adopts increasingly more negative values. To sum up, pores with small relative volume changes tend to become more regular, and pores with large relative volume changes tend to become more irregular.
3. The stress over the whole plastic region of the HPDC cast samples increases by about 31.5 MPa after the hydrostatic pressure treatment. Work hardening rates are, however, not seen to be affected significantly.
4. FE simulations successfully capture the bimodal distribution of the relative volume change after pressurization, albeit the average value of the second $\Delta V/V_0$ peak is lower than the one measured experimentally. A good agreement between the dis-

tributions of the relative change in the *CF* is found between the XCT measurements and the simulations. Only the pores undergoing pore size reductions higher than 45 pct (final pore volumes smaller than 3500 μm^3), for which the $\Delta CF/CF_0$ adopts the largest negative values, are not captured by the model. It is proposed that the source of this discrepancy resides in the inherent plastic anisotropy of hcp Mg, that manifests itself especially when the pore size is of the same order of magnitude than the grain size. The simple J_2 plasticity model used here cannot capture this phenomenon and a crystal plasticity model with adequate grain orientation would be needed. Despite this drawback, the model successfully predicts quantitatively the beneficial effect of the high pressure treatment on the yield stress of the HPDC casting.

5. Neighboring pores are observed to have a very strong effect on the evolution of the porosity during the pressure treatment, so that the pores having close neighbors of relatively larger size suffer a larger size reduction than isolated pores and/or pores whose closest neighbors are relatively smaller. This is particularly true for the pore population with the largest volumes, while they remained relatively insensitive for the smallest pores, more influenced by the local crystal anisotropy.

REFERENCES

1. M. Bamberger and J. Dehm: *Annu. Rev. Mater. Res.*, 2008, vol. 38, pp. 505–33.
2. B.L. Mordike and T. Ebert: *Mater. Sci. Eng. A*, 2001, vol. 302, pp. 37–45.
3. M. Easton, A. Beer, M.R. Barnett, C. Davies, G. Dunlop, Y. Durandet, S. Blacket, T. Hilditch, and P. Beggs: *JOM*, 2008, vol. 60 (11), pp. 57–62.
4. D. Letzig, J. Swiostek, J. Bohlen, P.A. Beaven, and K.U. Kainer: *Mater. Sci. Technol.*, 2008, vol. 24 (8), pp. 991–96.
5. A. Hamasaiid, G. Dour, T. Loulou, and M.S. Dargusch: *Int. J. Therm. Sci.*, 2010, vol. 49, pp. 365–72.
6. N.A. El-Mahallawy, M.A. Taha, E. Pokora, and F. Klein: *J. Mater. Proc. Technol.*, 1998, vol. 73, pp. 125–38.
7. E.M. Gutman, Ya. Unigovski, M. Levkovich, Z. Koren, E. Aghion, and M. Dangur: *Mater. Sci. Eng. A*, 1997, vols. 234–236, pp. 880–83.
8. S.G. Lee, A.M. Gokhale, G.R. Patel, and M. Evans: *Mater. Sci. Eng. A*, 2006, vol. 427, pp. 99–111.
9. J.P. Weiler, J.T. Wood, R.J. Klassen, R. Berkmortel, and G. Wang: *Mater. Sci. Eng. A*, 2006, vol. 419, pp. 297–305.
10. J.P. Weiler and J.T. Wood: *J. Alloys Compd.*, 2012, vol. 537, pp. 133–40.
11. J.P. Weiler and J.T. Wood: *Mater. Sci. Eng. A*, 2009, vol. 527, pp. 25–31.
12. J.P. Weiler and J.T. Wood: *Mater. Sci. Eng. A*, 2009, vol. 527, pp. 32–37.
13. J.P. Weiler, J.T. Wood, R.J. Klassen, E. Maire, R. Berkmortel, and G. Wang: *Mater. Sci. Eng. A*, 2005, vol. 395, pp. 315–22.
14. M.F. Horstemeyer, N. Yang, Ken Gall, D.L. McDowell, J. Fan, and P.M. Gullett: *Acta Mater.*, 2004, vol. 52, pp. 1327–36.
15. S.G. Lee, G.R. Patel, A.M. Gokhale, A. Sreeranganathan, and M.F. Horstemeyer: *Mater. Sci. Eng. A*, 2006, vol. 427, pp. 255–62.
16. S.G. Lee, G.R. Patel, A.M. Gokhale, A. Sreeranganathan, and M.F. Horstemeyer: *Scripta Mater.*, 2005, vol. 53, pp. 851–56.
17. G. Chaha, J.E. Allison, and J.W. Jones: *Metall. Mater. Trans. A*, 2007, vol. 38A, pp. 286–97.
18. C.D. Lee: *J. Mater. Sci.*, 2007, vol. 42, pp. 10032–39.
19. J. Song, S.M. Xiong, M. Li, and J. Allison: *J. Alloys. Compd.*, 2009, vol. 477, pp. 863–69.
20. C.H. Cáceres and B.I. Selling: *Mater. Sci. Eng. A*, 1996, vol. 220, pp. 109–16.
21. C.H. Cáceres: *Scripta Metall. Mater.*, 1995, vol. 32, pp. 1851–56.
22. B. Chen, Q. Yuan, J. Luo, and J.H. Fan: *Trans. Nonferrous Met. Soc. China*, 2010, vol. 20, pp. s467–70.
23. S.G. Lee, A.M. Gokhale, and A. Sreeranganathan: *Mater. Sci. Eng. A*, 2006, vol. 427, pp. 92–98.
24. G. Nicoletto, G. Anzelotti, and R. Konečná: *Proc. Eng.*, 2010, vol. 2, pp. 547–54.
25. N. Vanderesse, E. Maire, A. Chabod, and J.Y. Buffiére: *Int. J. Fatigue*, 2011, vol. 33, pp. 1514–25.
26. S.B. Biner and W.A. Spitzig: *Acta Metall. Mater.*, 1990, vol. 4, pp. 603–10.
27. A.K. Vasudevan and O. Richmond: *Mater. Sci. Eng. A*, 1989, vol. 107, pp. 63–69.
28. A.L. Gurson: Ph.D. Thesis, Division of Engineering, Brown University, Providence, RI, 1975.
29. A.L. Gurson: *J. Eng. Mater. Technol.*, 1977, vol. 99 (1), pp. 2–15.
30. I.E. French and P.F. Weinrich: *Acta. Metall. Mater.*, 1973, vol. 21, pp. 1533–37.
31. W.A. Spitzig: *Acta. Metall. Mater.*, 1990, vol. 38, pp. 1445–53.
32. S. Biswas, F. Sket, M. Chiumenti, I. Gutiérrez-Urrutia, J.M. Molina-Aldareguía, and M.T. Pérez-Prado: *Metall. Mater. Trans. A*, 2013, vol. 44A, pp. 4391–403.
33. L.A. Feldkamp, L.C. Davis, and J.W. Kress: *J. Opt. Soc. Am. A*, 1984, vol. 1, pp. 612–19.
34. W Niblack: *An Introduction to Digital Image Processing*, Prentice Hall, Upper Saddle River, NJ, 1986, pp. 115–16.
35. E.J. Garboczi: *Cement Concrete Res.*, 2002, vol. 32, pp. 1621–38.
36. A. Isaac, F. Sket, W. Reimers, B. Camin, G. Santhoff, and A.R. Pyzalla: *Mater. Sci. Eng. A*, 2008, vol. 478, pp. 108–18.
37. http://www-sop.inria.fr/asclepios/software/MedINRIA/, accessed April 2015.
38. K. Dzieciol, A. Borbèly, F. Sket, A. Isaac, M. Di Michiel, P. Cloetens, Th. Buslaps, and A.R. Pyzalla: *Acta Mater.*, 2011, vol. 59, pp. 671–77.
39. K. Dzieciol, A. Isaac, F. Sket, A. Borbèly, and A.R. Pyzalla: *Proc. EPD Congr., Characterization of Minerals, Metals and Materials*, San Francisco, CA, 2009, pp. 15–19.
40. http://www.volumegraphics.com/products/vgstudio-max/basic-functionality/, accessed April 2015.
41. S. Youssef, E. Maire, and R. Gaertner: *Acta Mater.*, 2005, vol. 53, pp. 719–30.
42. http://www.altairhyperworks.com/Product,7,HyperMesh.aspx, accessed April 2015.
43. Abaqus/Standard, Dassault Systèmes, 2011, http://www.simulia.com, accessed April 2015.
44. http://www.matweb.com/search/DataSheet.aspx?MatGUID=6a9fb156317c4ca8ab00bf8443eb13b3, accessed April 2015.

45. C.D. Lee: *Mater. Sci. Eng. A*, 2007, vols. 454–455, pp. 575–80.
46. C. Bettles and M.R. Barnett: *Advances in Wrought Magnesium Alloys*, Woodhead Publishing, Oxford, 2012.
47. M.R. Barnett: *Metall. Mater. Trans. A*, 2003, vol. 34A, pp. 1799–806.
48. R.W. Rice: *J. Mater. Sci.*, 1997, vol. 32, pp. 4731–36.
49. V. Tvergaard: *J. Mech. Phys. Solids.*, 1996, vol. 8, pp. 1237–53.
50. V. Tvergaard and C. Niordson: *Int. J. Plast.*, 2004, vol. 20, pp. 107–20.
51. J.W. Hutchinson: *Int. J. Solids. Struct.*, 2000, vol. 37, pp. 225–38.